

## High-Energy Gamma Rays from Spontaneous Fission of $^{238}\text{U}^\dagger$

H. W. Sobel, A. A. Hruschka, W. R. Kropp, J. Lathrop, and F. Reines

*University of California, Irvine, California 92664*

and

M. F. Crouch

*Case Western Reserve University, Cleveland, Ohio 44106*

and

B. S. Meyer\* and J. P. F. Sellschop

*University of the Witwatersrand, Republic of South Africa*

(Received 17 August 1972)

A large shielded liquid-scintillation detector operating 3240 m below the surface of the earth was used to detect  $\gamma$  rays from the spontaneous fission of a  $^{238}\text{U}$  source. In an energy range from 8 to 20 MeV, the derived spectrum is:  $N(E) = (6.99 \pm 0.60) \times 10^{-1} e^{-E/1.41 \pm 0.12}$  photons fission $^{-1}$  MeV $^{-1}$ .

### I. INTRODUCTION

The apparatus with which the measurement was performed was originally designed for the detection of solar neutrinos by elastic scattering of electrons. The shield was primarily intended to attenuate the flux of neutrons produced by spontaneous fission of  $^{238}\text{U}$  in the rock surrounding the detector. However, as the experiment progressed, it became clear that our major source of background was  $\gamma$  rays. The shield was insufficient to reduce this background to levels which would permit the observation of solar neutrinos. The level we were striving for was, of course, quite small since the predicted count rate using a flux at the earth of  $2.4 \times 10^7$   $\nu/\text{sec cm}^2$  was only about 20 events per year with energy  $\geq 6$  MeV.

We suspected that the high-energy background was due to  $\gamma$  rays from the spontaneous fission of  $^{238}\text{U}$  found in rock surrounding our detector. In order to investigate this background further, we obtained a  $10^4$ -g uranium metal source.<sup>2</sup> This large quantity was necessary to obtain reasonable count rates in the high-energy region. The source was in the form of many thin disks to reduce self-absorption. With this source inside the shield, we observed a source-associated signal extending to  $>20$  MeV.

The  $\gamma$  spectrum from  $^{238}\text{U}$  fission was previously measured up to 7 MeV.<sup>3,4</sup> If indeed, we were observing fission  $\gamma$  rays, we could extend this spectrum considerably.

We were fortunate in having a detector which was large enough to be compatible with our necessarily large source dimensions. In addition, the deep underground location of our detector provided an experimental environment which allowed the cosmic-ray background to be ignored.

### II. APPARATUS

The detector was a 6-ft-long,  $5\frac{1}{2}$ -ft-diam aluminum tank (Fig. 1), which contained 1000 gal of mineral-oil-based liquid scintillator.<sup>5</sup> The two ends of the cylinder were sealed with  $\frac{3}{4}$ -in.-thick Perspex windows. The cylinder was lined along its cylindrical wall with a series of Perspex-air-Perspex sandwiches. The sandwiches assured total internal reflection of the scintillator photons, and with the addition of an opaque sheeting inside the sandwich, divided the tank internally into five sections (Fig. 2). The cylinder was viewed on both ends by a total of 58, 5-in. Dumont photomultiplier tubes (PMT). The tubes were separated from the Perspex window by a 12-in. air gap to make the response of the detector more uniform. Each of the four outer sections had six tubes on each end, while the inner section had five tubes on each end.

A block diagram of the electronics is given in Fig. 3. Each PMT had an emitter follower mounted on its base to drive the 35-ft-long coaxial cable which led to the electronics shack. The signals from each section were divided into four groups, A, B, C, and D. In each of the four outer sections, a group consisted of three tubes. The center section had only ten tubes, so, while it contributed the standard three tubes to each of groups A and B, it contributed only two tubes to each of groups C and D. The individual groups were amplified, and the amplifier outputs fanned out into two branches. On one branch, the four groups from one section were recombined to form a section sum pulse and then stored in delay lines. On the other branch, all the five A groups were combined, and similarly, the other groups, so as to result in the 58 tubes divided into 4 large

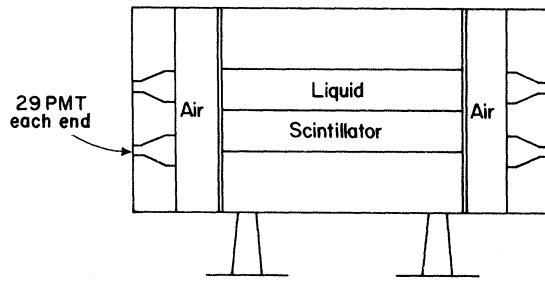


FIG. 1. Schematic of the detector.

groups. Each of these went through a discriminator, a shaper, and finally to a fourfold coincidence circuit. If the four pulses overlapped with a resolving time of  $0.1 \mu\text{sec}$ , a prompt trigger was generated along with two delayed triggers and various signals to control circuits and blocks.

After being stored in delay lines, the section sum pulses went to a Tektronix type-551 dual-beam oscilloscope. A type-M linear-gate plug-in handled three of the pulses, while a type-CA handled the remaining two. The prompt trigger began the sweeps of both beams. The delayed triggers switched the type-M unit twice and the type-CA once, so that one trace had three pulses and the other two. This arrangement minimizes PMT noise pulses. Both traces were recorded on a single frame of 35-mm Kodak type-2475 film by an oscilloscope camera which had its shutter removed. When the display was complete, the camera was advanced to the next frame.

Perspex tubes, which went from the outside of the detector to the center of each section (Fig. 4) served as a pathway for a light pulser<sup>6</sup> with which the PMT's were balanced. Since the PMT high voltage originated from a single supply, the individual tube gains were adjusted with series resistors.

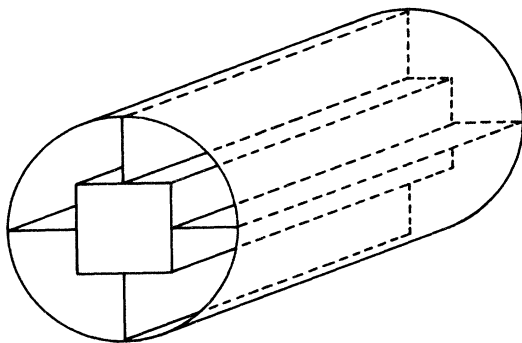


FIG. 2. Schematic of the detector sections.

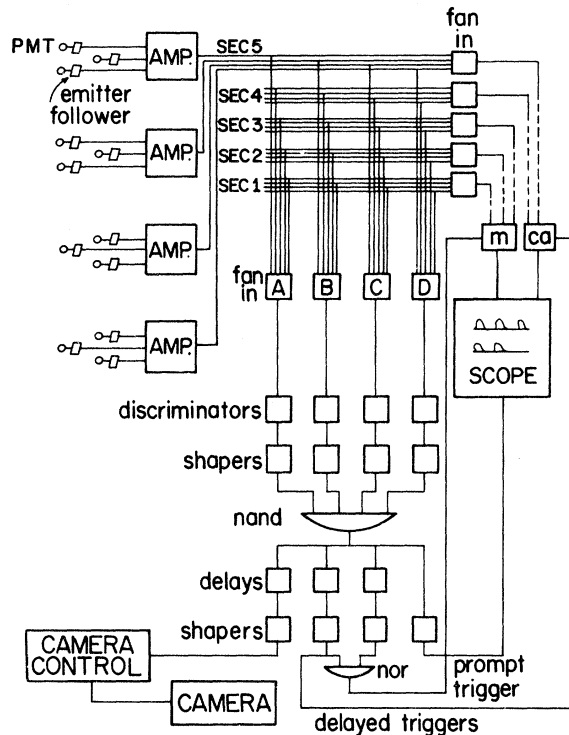


FIG. 3. Schematic diagram of the electronics.

Energy calibration was by means of an  $^{88}\text{Y}$  source placed in the center of the individual sections via the aforementioned Perspex tubes. The sum pulse of a given section was fed into a pulse-height analyzer and the peak voltage was determined. This peak was taken to be the total absorption energy of 2.76 MeV. Tube drift and/or loss was determined by observing the position of such a peak for each section. By moving the source along the length of a section and recording the pulse height

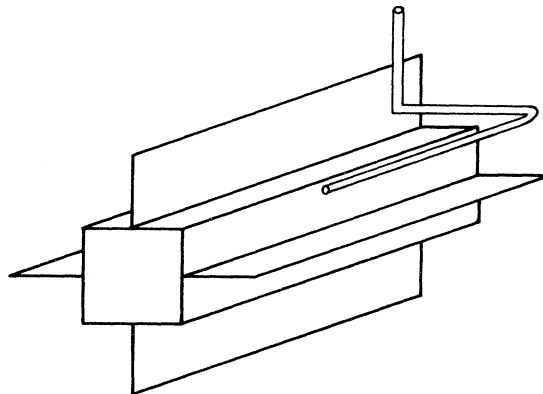


FIG. 4. Schematic of the detector interior showing the location of a Perspex access tube.

of the tubes at one end of a section as a function of position, we obtained a relative response function (Fig. 5). Since attenuation was relatively linear from end to end, when all the tubes of a section were added, it was possible to get quite a flat response (Fig. 6).

The detector was located 10 638 ft below the surface in the East Rand Proprietary Mine gold mine outside Johannesburg, South Africa. The chamber in which the detector was located is part of a long tunnel. At our site, the tunnel is 20 ft wide and arches to about 10 ft high. The walls were concrete, and about 6 in. thick.

The entire detector was surrounded by a shield consisting of a 2-in.-thick layer of boric acid in polyethylene tubing, and a 2–3-ft-thick wax block wall weighing approximately 45 tons. The shield was enclosed in a wooden retaining wall, since the high temperature on the site in combination with the shield's own considerable weight caused the wax to flow (Fig. 7).

### III. METHOD

The uranium source is a copious producer of neutrons, in addition to the fission  $\gamma$  rays we were trying to observe. These neutrons can be seen in the detector directly by means of knock-on protons in the liquid scintillator or the neutrons can be captured in the aluminum and iron of the detector environment producing capture- $\gamma$  rays. The  $\gamma$  rays from thermal capture in aluminum and iron can be as large as 7.72 and 10.16 MeV, respectively.<sup>7, 8</sup> Thus, if the kinetic energy of the incident neutron is added to these  $\gamma$  energies, it is possible to get higher  $\gamma$  energies as a result.

We had available for analysis the following experimental measurements (the source locations

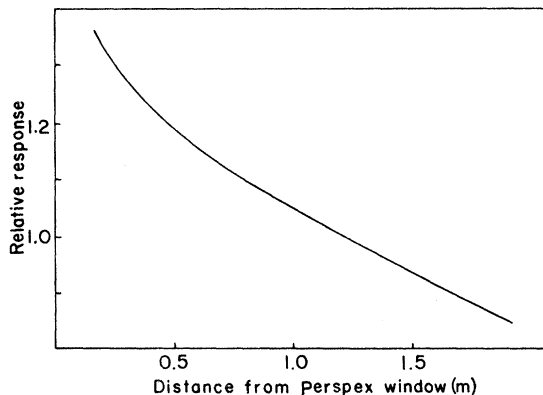


FIG. 5. Response function of a single detector section as observed by six PMT's at one end.

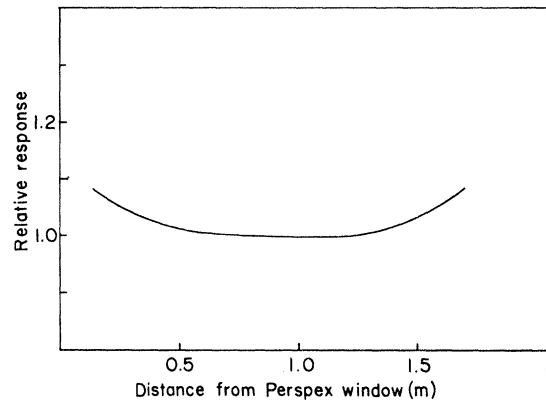


FIG. 6. Response function of a single detector section as observed by PMT's at both ends.

are shown in Fig. 7):

- (1) a run of 5.9 h with the uranium metal inside the shield and the discriminators set at 8 MeV;
- (2) a run of 162.12 h with the uranium metal inside the shield and the discriminators set at 12 MeV;
- (3) a run of 37.22 h with the uranium metal outside the shield and the discriminators set at 8 MeV;
- (4) a run of 0.28 h with a Pu-Be source outside the shield and the discriminators set at 8 MeV;
- (5) a background run of 213.72 h with the discriminators set at 8 MeV.

Our data with uranium metal inside the shield are used to determine the spectrum of photons per fission. The experimental spectrum must have the background subtracted from it, and must be corrected for detector aperture, resolution,

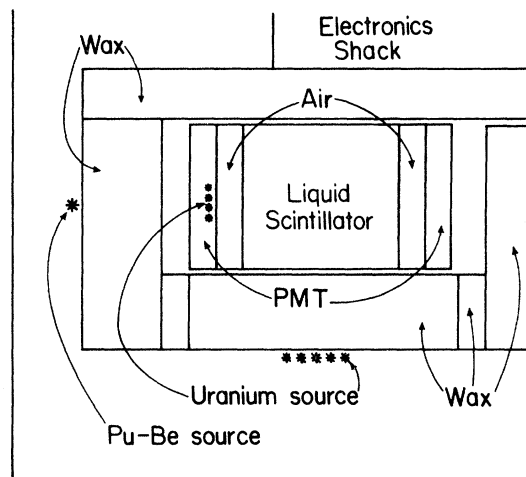


FIG. 7. Schematic diagram of the experimental site showing source locations.

efficiency, and self-absorption.

U and Pu-Be source measurements in other locations about the detector were used to correct for the possible effects of direct neutrons from the source and  $\gamma$  rays produced by neutron capture in the surroundings.

A. Uranium Inside Shield

The observed data were obtained by adding detector runs with two different minimum discriminator settings, 8 and 12 MeV. These points plotted on semilog paper evidently fell about a straight line, which implied an exponential solution (Fig. 8). The maximum-likelihood technique was employed to solve for the parameters of the exponential.<sup>9</sup> In this solution, the lowest energy bin in each run was neglected, as a discriminator cutoff effect was evident. In Fig. 8, we have plotted the results of this procedure superimposed upon the observed points. Figure 9 is the integral spectrum derived from this result.

We have 42 mole of  $^{238}\text{U} = 2.5 \times 10^{25}$  atoms. The partial half-period ( $\tau_{1/2}$ ) for spontaneous fission of  $^{238}\text{U} = 10^{16}\text{yr}$ <sup>10</sup>:

$$\frac{dn}{dt} = \frac{-n}{\tau_{1/2}} \ln 2 = 2.0 \times 10^5 \frac{\text{fissions}}{\text{h}}$$

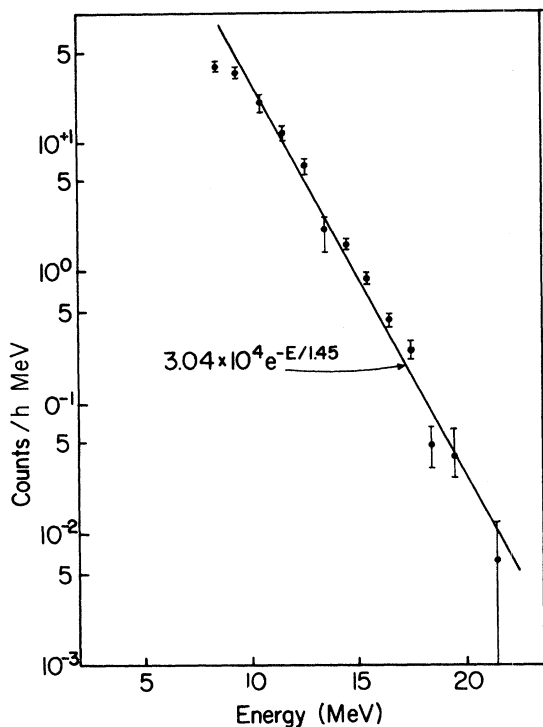


FIG. 8.  $\gamma$  spectrum for uranium inside the shield. The maximum likelihood line is fitted to observed data points.

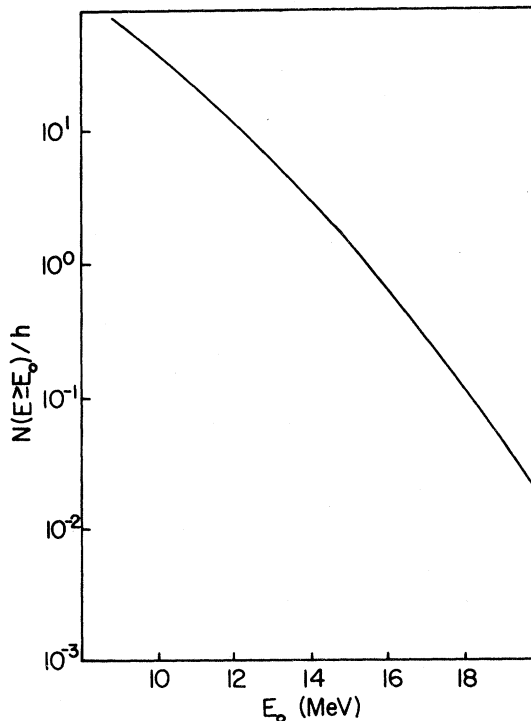


FIG. 9. Uranium inside shield. Integral  $\gamma$  spectrum is fitted to observed data.

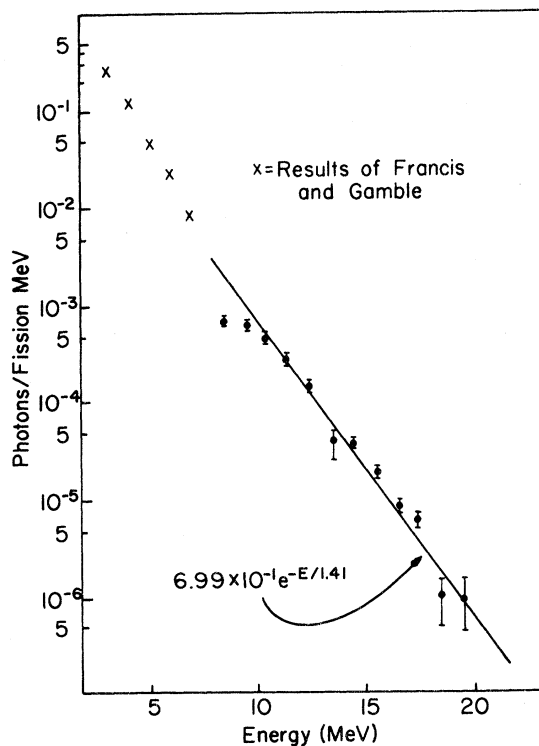


FIG. 10. Photons/fission MeV versus photon energy.

In Appendix I we calculate the corrections to the spectrum due to resolution, efficiency, detector aperture, and source self-absorption. Using these corrections and the above, we get:

$$\frac{\text{photons}}{\text{fission}} = \frac{4\pi}{4.01} \frac{1}{0.6} \frac{0.86}{2.0 \times 10^5} 3.13 \times 10^4 e^{-E/1.41}$$

$$= (6.99 \pm 0.60) \times 10^{-1} e^{-E/1.41 \pm 0.12}$$

The resultant curve is compared (Fig. 10) with the results of Francis and Gamble<sup>3</sup> which extended to 7 MeV.

#### B. Knock-On Protons

The specific luminescence of protons in an organic scintillator is less than that of electrons. In Fig. 11, we plot the pulse height vs energy for electrons and protons.<sup>11</sup> If we look at events in our detector whose energy is  $\geq 8$  MeV, for example, we would need neutron energies  $\geq 14$  MeV.

We observe  $N(E) = 3.13 \times 10^4 e^{-E/1.41} \text{h}^{-1}$ . Correcting this to  $4\pi$  solid angle, we get:

$$N(E \geq 8 \text{ MeV}) = \int_8^{\infty} \frac{3.13 \times 10^4}{0.319} e^{-E/1.41} dE$$

$$= 4.7 \times 10^2 / \text{h} = 1.3 \times 10^{-1} / \text{sec}.$$

However, we have  $6 \times 10^{-3}$  neutrons/sec coming from our uranium source with  $E \geq 14$  MeV.<sup>9</sup> Thus, we observe a rate  $(1.3 \times 10^{-1}) / (6.0 \times 10^{-3}) = 21.6$  times larger than the number of available neutrons. Or, the knock-on proton contribution to our signal at energies  $\geq 8$  MeV is less than 4.6%.

#### C. Comparison of Spectrum Observed with Uranium Inside Shield to that Observed with Uranium Outside Shield

By normalizing to  $4\pi$  solid angle, the spectrum we observe with the uranium inside the shield,

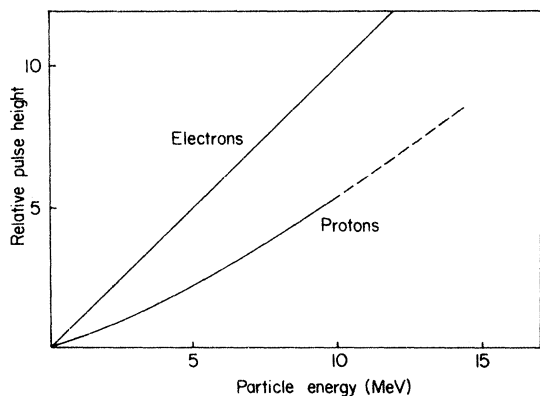


FIG. 11. Relative luminescence of electrons and protons in an organic scintillator.

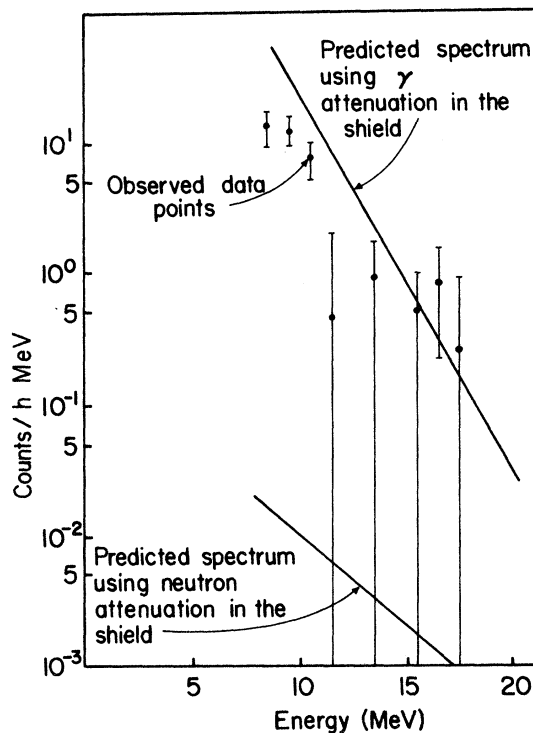


FIG. 12. Comparison of the observed spectrum for uranium outside the shield to those predicted by  $\gamma$  and neutron attenuation in the shield.

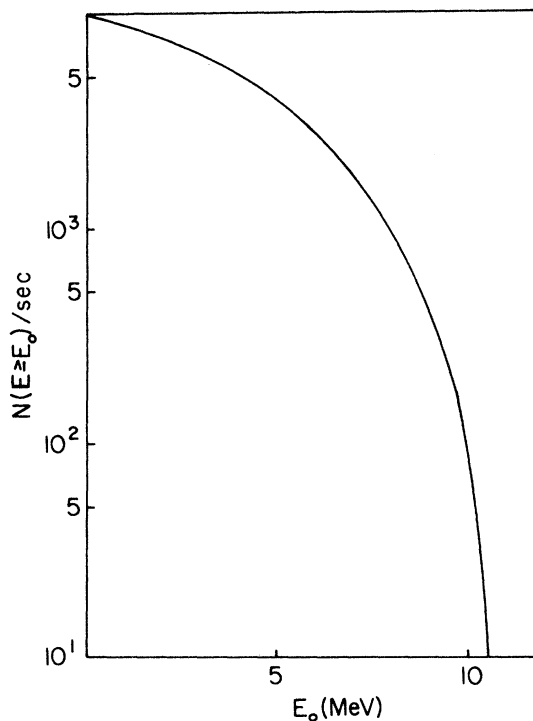


FIG. 13. Integral spectrum of neutrons from our Pu-Be source.

we get the spectrum emanating from the source. The source is now placed outside the shield. The spectrum we then observe can be compared with that predicted by  $\gamma$ -ray and neutron attenuation in the shield. The observed and predicted spectra are plotted in Fig. 12.

The predicted curve using single  $\gamma$  attenuation reasonably fits the data, while the curve predicted by neutron attenuation is much too small. From this result, we can eliminate the mode in which both the inside uranium and the outside uranium produce neutrons which are captured in the supports of the detector inside the shield.

However, we are still left with the possibility of the capture of neutrons outside the shield and the  $\gamma$  rays, so produced, penetrating the shield.

At this point, we can also discuss the possible multiplicity of our observed spectrum. Here, for example, a 16-MeV pulse could be caused by the pileup of two 8-MeV  $\gamma$  rays. If this were the case, when the source was moved from one position to another, the rate would be proportional to the square of the ratio of the respective solid-angle factors. In addition, an 8-MeV  $\gamma$  ray is attenuated more in our shield than a 16-MeV  $\gamma$  ray. These two factors would combine to produce an extra attenuation factor of  $\sim 23$  when the source is moved

from inside to outside the shield. This is not observed.

The poor statistics of our "uranium outside" data do not allow us to reject some small contribution ( $\lesssim 25\%$ ) of multiple  $\gamma$  rays.

#### D. Comparison of Rate with Uranium Outside Shield to Rate with Pu-Be Outside Shield

If we assume that the spectrum we observe in the detector when the uranium source is outside the shield is due entirely to neutrons being captured in the surrounding concrete, then we can predict the observed rate with a Pu-Be source outside the detector.

We assume that the neutrons from each source undergo the same capture processes in the concrete. Of all the elements in the environment surrounding the detector, silicon (which is a primary component of the concrete) has the largest capture- $\gamma$  energy.<sup>7</sup> For thermal neutrons,  $^{28}\text{Si}(n, \gamma)^{29}\text{Si}$  has a  $\gamma$  energy of 8.475 MeV, and  $^{29}\text{Si}(n, \gamma)^{30}\text{Si}$  has a  $\gamma$  energy of 10.617 MeV.<sup>8</sup>

We first assume that all the captures occur in  $^{28}\text{Si}$  and write:

$$N(E \geq E')_{\text{Pu-Be}}^{\text{Pred.}} = \frac{N_n(E \geq E_0)_{\text{Pu-Be}}}{N_n(E \geq E_0)_{^{238}\text{U}}} \times \frac{\Omega_{\text{Pu-Be}}}{\Omega_{^{238}\text{U}}} \times \text{Shielding Factor} \times N(E \geq E')_{^{238}\text{U}}^{\text{Obs.}}$$

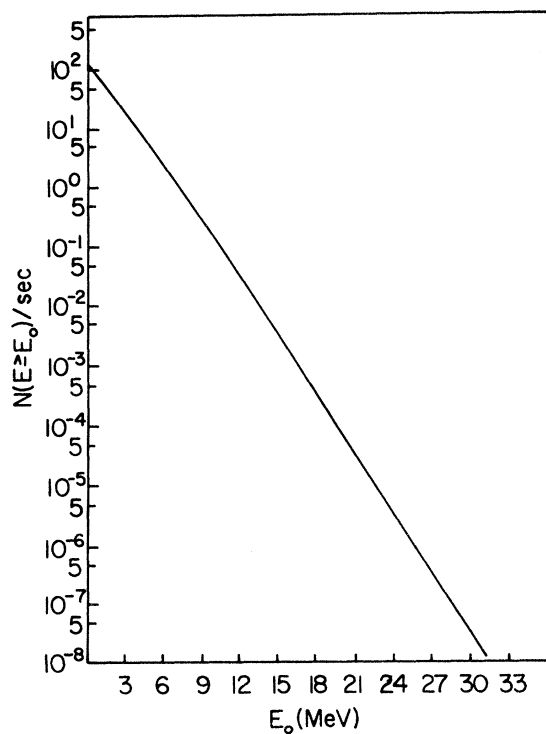


FIG. 14. Integral spectrum of neutrons from  $10^4$  g of uranium metal.

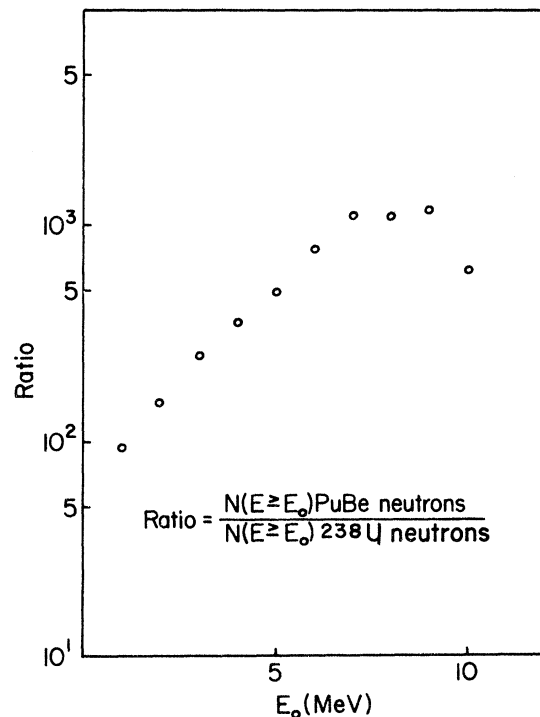


FIG. 15. Available neutron ratio versus neutron energy.

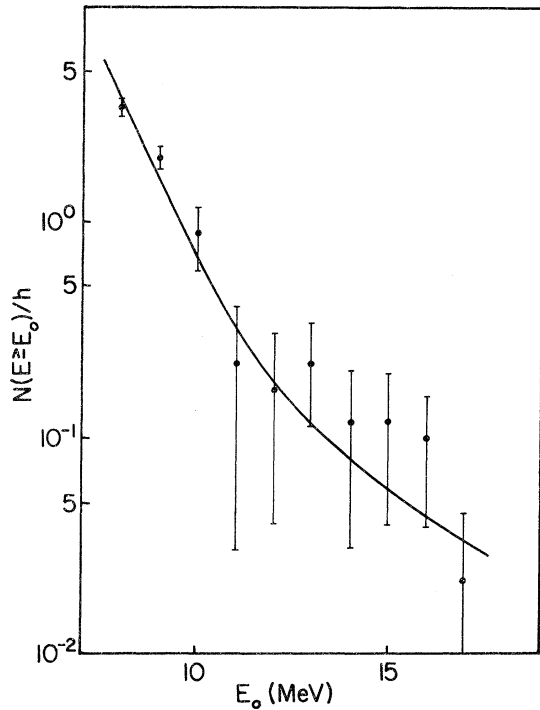


FIG. 16. Observed rate with uranium outside the shield (background subtracted).

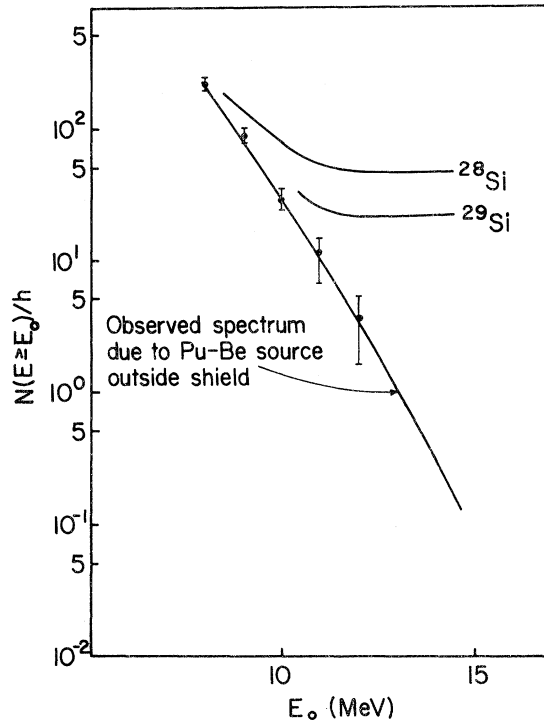


FIG. 17. Observed spectrum due to the Pu-Be source outside the shield compared to the predicted spectra.

where  $N(E \geq E')$ <sub>Pu-Be</sub><sup>Pred.</sup> equals the predicted rate in the detector with energy  $\geq E'$  due to a Pu-Be source outside the shield;  $N_n(E \geq E_0)$ <sub>Pu-Be</sub> equals the rate of neutrons coming from the Pu-Be source with energy  $\geq E_0$  (Fig. 13);  $N_n(E \geq E_0)$ <sub>238U</sub> equals the rate of neutrons coming from the uranium source with energy  $\geq E_0$  (Fig. 14);  $[N_n(E \geq E_0)$ <sub>Pu-Be</sub>]/ $[N_n(E \geq E_0)$ <sub>238U</sub>] equals ratio plotted versus  $E_0$  in Fig. 15;  $E_0 = E' - 8.5$  MeV (for captures in <sup>28</sup>Si);  $\Omega$ <sub>Pu-Be</sub>

equals the solid angle subtended by the detector at the concrete which has been irradiated with neutrons from the Pu-Be source<sup>9</sup>;  $\Omega$ <sub>238U</sub> equals the solid angle subtended by the detector at the concrete which has been irradiated with neutrons from the uranium source<sup>9</sup>; Shielding Factor equals a factor to compensate for the difference in shielding which is seen by the Pu-Be-induced  $\gamma$  rays and the uranium-induced  $\gamma$  rays;  $N(E \geq E')$ <sub>Obs.</sub><sup>238U</sup>

TABLE I. Predicted Pu-Be rate based on neutron captures in <sup>28</sup>Si.

$E'$	<sup>238</sup> U $N(E \geq E')/h$ observed	Neutron ratio $\frac{N(E \geq E_0)_{\text{Pu-Be}}}{N(E \geq E_0)_{238\text{U}}}$	Solid-angle factor	Shield factor	Pu-Be $N(E \geq E')/h$ predicted	Pu-Be $N(E \geq E')/h$ observed	Observed/ predicted
8.5	$2.5 \times 10^0$	$7.0 \times 10^1$	0.755	1.30	172.0	130.00	0.756
9.0	$1.8 \times 10^0$	$8.0 \times 10^1$	0.755	1.29	140.0	86.00	0.614
9.5	$1.2 \times 10^0$	$9.4 \times 10^1$	0.755	1.28	109.0	50.00	0.459
10.0	$7.0 \times 10^{-1}$	$1.2 \times 10^2$	0.755	1.27	80.5	31.00	0.385
10.5	$4.5 \times 10^{-1}$	$1.5 \times 10^2$	0.755	1.26	64.2	18.00	0.280
11.0	$3.0 \times 10^{-1}$	$1.8 \times 10^2$	0.755	1.25	51.0	10.00	0.196
11.5	$2.3 \times 10^{-1}$	$2.2 \times 10^2$	0.755	1.24	47.4	6.00	0.127
12.0	$1.8 \times 10^{-1}$	$2.8 \times 10^2$	0.755	1.24	47.2	3.50	0.074
12.5	$1.4 \times 10^{-1}$	$3.5 \times 10^2$	0.755	1.23	45.5	2.00	0.044
13.0	$1.2 \times 10^{-1}$	$4.3 \times 10^2$	0.755	1.22	47.5	1.00	0.021
13.5	$1.0 \times 10^{-1}$	$4.8 \times 10^2$	0.755	1.22	44.2	0.60	0.014
14.0	$8.0 \times 10^{-2}$	$6.2 \times 10^2$	0.755	1.22	45.7	0.30	0.007
14.5	$6.8 \times 10^{-2}$	$7.4 \times 10^2$	0.755	1.22	46.3	0.15	0.003

TABLE II. Predicted Pu-Be rate based on neutron captures in  $^{238}\text{U}$ .

$E'$	$^{238}\text{U}$ $N(E \geq E')/h$ Observed	Neutron ratio $\frac{N(E \geq E_0)_{\text{Pu-Be}}}{N(E \geq E_0)_{^{238}\text{U}}}$	Solid- angle factor	Shield factor	Pu-Be $N(E \geq E')/h$ predicted	Pu-Be $N(E \geq E')/h$ observed	Observed/ predicted
10.5	$4.5 \times 10^{-1}$	$7.0 \times 10^1$	0.755	1.26	30.0	18.00	0.600
11.0	$3.0 \times 10^{-1}$	$8.0 \times 10^1$	0.755	1.25	22.7	10.00	0.441
11.5	$2.3 \times 10^{-1}$	$9.4 \times 10^1$	0.755	1.24	20.2	6.00	0.297
12.0	$1.8 \times 10^{-1}$	$1.2 \times 10^2$	0.755	1.24	20.2	3.50	0.173
12.5	$1.4 \times 10^{-1}$	$1.5 \times 10^2$	0.755	1.23	19.5	2.00	0.103
13.0	$1.2 \times 10^{-1}$	$1.8 \times 10^2$	0.755	1.22	19.9	1.00	0.050
13.5	$1.0 \times 10^{-1}$	$2.2 \times 10^2$	0.755	1.22	20.3	0.60	0.030
14.0	$8.0 \times 10^{-2}$	$2.8 \times 10^2$	0.755	1.22	20.6	0.30	0.015
14.5	$6.8 \times 10^{-2}$	$3.5 \times 10^2$	0.755	1.22	21.9	0.15	0.007

equals the observed rate in the detector with energy  $\geq E'$  due to the uranium source outside the shield (Fig. 16). The factors in this equation are tabulated in Table I along with the ratio of observed Pu-Be rate to predicted Pu-Be rate. The same equation with  $E_0 = E' - 10.6$  MeV [ $^{29}\text{Si}(n, \gamma) - ^{30}\text{Si}$ ] is tabulated in Table II.

From these ratios, we can put limits on the fraction of the observed uranium-outside spectrum, which can be accounted for by capture- $\gamma$  rays. For  $E' = 12.5$  MeV, for example, between 4.4 and 10.3% of the signal may be due to capture- $\gamma$  rays. The observed Pu-Be spectrum and the predicted spectra in these two cases are plotted in Fig. 17.

#### E. Comparison of Rate with Uranium Inside Shield to Rate with Pu-Be Outside Shield

In order to put some limit on the number of  $\gamma$  rays from neutron capture which contribute to

our observed signal when the uranium source is inside the shield, we can compare this signal to that observed when the Pu-Be source is outside the shield. In this comparison, the neutrons from the uranium can be captured in the aluminum shell of the detector or in the iron superstructure around the detector. The neutrons from the Pu-Be source can only be captured in the rock. Since the different capturing media and amounts of these media are involved, some probability of  $\gamma$  production must be determined in each case. This is done in Appendix III, and we get:

$$\frac{\text{Prob. of } \gamma\text{'s due to Pu-Be}}{\text{Prob. of } \gamma\text{'s due to uranium}} = \frac{1.16 \times 10^{-2}}{3.41 \times 10^{-5}} = 3.4 \times 10^2.$$

If we attribute all of the events we observe from the uranium source to neutron captures in aluminum, then we can predict the rate we should observe due to neutrons from the Pu-Be source being captured in the rock:

$$\text{Pu-Be } N(E \geq 8.5 \text{ MeV})/h \text{ Predicted} = \left( \begin{array}{c} \text{Ratio of} \\ \text{observable} \\ \gamma\text{-} \\ \text{production} \\ \text{probability} \end{array} \right) \left( \begin{array}{c} \text{Available} \\ \text{neutron} \\ \text{ratio} \end{array} \right) \left( \begin{array}{c} \text{Solid-} \\ \text{angle} \\ \text{factor} \end{array} \right) \\ \times \left( \begin{array}{c} \text{Shield} \\ \text{factor} \end{array} \right) \left( \begin{array}{c} ^{238}\text{U} \\ N(E \geq 8.5 \text{ MeV})/h \\ \text{observed} \end{array} \right).$$

*Available neutron ratio.* The uranium source must provide 0.8-MeV neutrons, while the Pu-Be source must provide thermal neutrons:

$$\frac{N(E \geq 0.025)_{\text{Pu-Be}}}{N(E \geq 0.8)_{\text{uranium}}} = \frac{10^4 \text{ (Fig. 13)}}{8 \times 10^1 \text{ (Fig. 14)}} = 1.25 \times 10^2.$$

*Solid-angle factor.* The solid angle subtended by the scintillator at the neutron-irradiated aluminum

is calculated to be 0.16.<sup>9</sup> The solid angle subtended by the scintillator at the neutron-irradiated rock is calculated to be 0.009 11.<sup>9</sup> The ratio is equal to:

$$\frac{\Omega(\text{Pu-Be})}{\Omega(\text{uranium})} = \frac{0.009 11}{0.16} = 0.057.$$

The shield factor is 1/4.04 (i.e., the Pu-Be-in-

duced  $\gamma$  rays see 2.5 ft of wax, while the uranium-induced  $\gamma$  rays see none).

The observed rate with uranium inside the shield is equal to (Fig. 9)

$$N(E \geq 8.5 \text{ MeV}) = 1 \times 10^2/\text{h}.$$

Thus we have

$$\begin{aligned} & \text{Pu-Be} \\ N(E \geq 8.5 \text{ MeV})/\text{h} \\ & \text{predicted} \\ & = \frac{(3.4 \times 10^2) (1.25 \times 10^2) (5.7 \times 10^{-2}) (1 \times 10^2)}{4.04} \\ & = 6.03 \times 10^4/\text{h}. \end{aligned}$$

We observe, however,  $1.5 \times 10^2/\text{h}$  with  $E \geq 8.5 \text{ MeV}$ .

In all of the above, we have assumed that single  $\gamma$  rays are produced in the neutron capture. This is, of course, not true, and in the case of the 8.5-MeV  $^{29}\text{Si}$  level, we know the transition probabilities. 3% go directly to the ground state.<sup>8</sup> Since the solid angle subtended by the detector at the rock is 0.24 rad, an extra attenuation of 51.4 is necessary to estimate the probability of both cascade  $\gamma$  rays intercepting the detector.

Let us assume that only the direct 8.5-MeV transitions would be observed from the rock, and further assume that the aluminum 8.5-MeV levels give *only* single transitions. These are the most conservative assumptions, as they predict the smallest Pu-Be rate.

So, we predict  $(3 \times 10^{-2}) (6.03 \times 10^4)/\text{h} = 1.81 \times 10^3/\text{h}$ . Since

$$\frac{\text{Observed Pu-Be rate}}{\text{Predicted Pu-Be rate}} = \frac{1.5 \times 10^2}{1.8 \times 10^3} = 8.3 \times 10^{-2},$$

we can say that not over 8.3% of the observed uranium signal with  $E \geq 8.5 \text{ MeV}$  is due to capture- $\gamma$  rays in aluminum.

The solid angle subtended by the iron at the source is  $\sim \frac{1}{10}$  of that for the aluminum. Therefore, the same type of result can be expected.

#### IV. CONCLUSION

We have been able to observe high-energy  $\gamma$  rays from a uranium source undergoing spontaneous fission. This has been accomplished because our experimental site is, for our purposes, free of cosmic-ray background and, because our detector is large enough to subtend a large solid angle at the source and thick enough to totally absorb a considerable fraction of the high-energy  $\gamma$  rays intercepting it.

The intercomparisons of observed spectra due to a Pu-Be neutron source and a uranium source in different locations show that:

(a) Direct neutron interactions in the scintillator account for less than 4.6% of our observed signal at energies  $\geq 8 \text{ MeV}$  (Sec. III).

(b) The observed rate with the uranium outside the shield cannot be due to neutrons being captured inside the shield (III).

(c) The observed rate with the uranium outside the shield can be from 25 to 60% due to capture- $\gamma$  rays at 10.5 MeV, but at higher energies, 13 MeV for example, only from 2 to 5% of the observed signal can be due to  $\gamma$  capture (III).

(d) The observed rate with the uranium inside the shield is less likely to be influenced by capture- $\gamma$  rays because of the type and amount of capturing material inside the shield. We calculate that not over 8.3% of the observed uranium signal with energies  $\geq 8.5 \text{ MeV}$  can be due to capture- $\gamma$  rays in aluminum (III).

Thus, the derived spectrum of photons/fission  $\times \text{MeV}$  from our uranium source is (from Sec. III):

$$N(E) = (6.99 \pm 0.60) \times 10^{-1} e^{-E/1.41 \pm 0.12}.$$

The calculation performed in Sec. III could have been more directly performed if a run was available with the Pu-Be neutron source inside our shield. Unfortunately, the need for this measurement was not realized until after the detector was dismantled.

Further study of these high-energy  $\gamma$  rays should, of course, be done on an element such as  $^{252}\text{Cf}$  where the half-life for spontaneous fission is about 14 orders of magnitude smaller than that for  $^{238}\text{U}$ . In this case, both the source and detector are so reduced in size that a table-top experiment at sea level becomes possible. This has, in fact, been done, and is reported in a companion paper.<sup>12</sup>

#### APPENDIX I: CORRECTIONS TO URANIUM INSIDE SHIELD DATA

##### 1. Resolution Correction

Having the functional form of the observed spectrum, we can correct it for detector resolution. The resolution of the detector was measured using a light pulser whose light output was varied. In Fig. 18, we have plotted the full width at half maximum of the detector response versus the energy equivalent of a light pulser output. A functional form was obtained for the observed points by assuming that the resolution was proportional to  $1/\sqrt{E}$ . The constant of proportionality was determined for the observed points, and the curve thus extrapolated to 20 MeV.

With this information resolution corrections were made,<sup>9</sup> and a spectrum of the actual energy

deposited in the tank was obtained. From the corrected spectrum we can deduce the number of photons per fission emanating from our source: The number of events per hour per MeV is

$$(3.13 \pm 0.27) \times 10^4 e^{-E/1.41 \pm 0.12}$$

### 2. Aperture of Detector

All the required solid-angle calculations were performed by dividing the detector and the relevant source into many small elements of area. The solid angle of each detector element and a sum of all such solid angles was then calculated. For example: If flux  $F_i$  comes from area  $S_i$  (Fig. 19), the amount penetrating area  $A_j$  is  $(A_j F_i) / (4\pi r_{ij}^2) \cos \star$  where  $\star$  is the angle between vector  $\vec{r}_{ij}$  and the normal to area  $A_j$ . Now,  $F_i = F / (S) S_i$  where  $F$  is the total flux from source;  $S$  is the total area of source. The total flux penetrating area  $A_j$  is

$$\sum_i \frac{A_j S_i}{4\pi r_{ij}^2} \frac{F}{S} \cos \star$$

The total flux penetrating area  $A$  is

$$\sum_{i,j} \frac{A_j S_i}{4\pi r_{ij}^2} \frac{F}{S} \cos \star$$

We calculate the fraction of the total flux originating at the source which penetrates area  $A$ :

$$\sum_{i,j} \frac{A_j S_i}{4\pi r_{ij}^2} \frac{1}{S} \cos \star$$

For this calculation, the detector surface is divided into 819 elements of area, and the source is divided into 87 elements of area. The result is that 0.319 of the total flux from the source intercepts the detector, or, the solid angle subtended by the detector at the uranium source is  $0.319(4\pi) = 4.01$  sr.

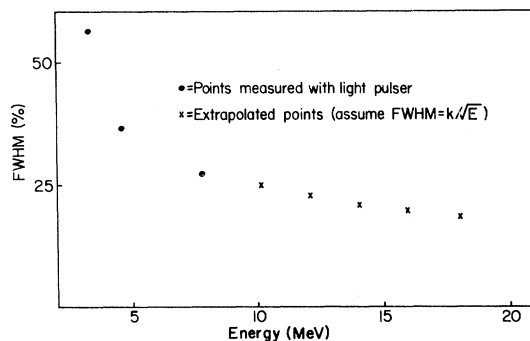


FIG. 18. Detector resolution (full width at half maximum) as measured with a light pulser versus energy.

### 3. Efficiency of Detector

In order to derive source characteristics from the observed spectrum, a measure of the total intrinsic efficiency of the detector is required. That is, the probability that a  $\gamma$  ray, after striking the detector surface, will lose all of its energy in the detector volume.

Total intrinsic efficiency calculations have been carried out for the case of a source on the axis of a cylindrical NaI detector.<sup>13</sup> This has been done with various source to crystal distances, for crystal diameters of 1.5 and 3 in.

These calculations are used to obtain a figure for the total intrinsic efficiency of our large liquid-scintillation detector. We look at a  $\gamma$  ray entering the NaI crystal such that the ratio of the crystal diameter to the Compton mean free path at that energy is the same as the ratio of our tank diameter to the Compton mean free path of a  $\gamma$  ray entering the liquid scintillator.

In choosing the  $\gamma$  energy which is incident upon the NaI crystal, we are careful to pick an energy at which the contribution of the photoelectric effect to the total cross section in NaI is approximately the same fraction as the contribution of pair production to the total cross section in the liquid scintillator.

For example, a 0.5-MeV  $\gamma$  ray in NaI has a Compton mean free path  $\lambda_C = 3.64$  cm and a mean free path for the photoelectric effect  $\lambda_{\text{photo}} = 23.7$  cm. For a crystal of diameter  $D = 7.6$  cm, we have  $D/\lambda_C = 2.09$ .

Our tank has a diameter  $D = 167$  cm, so the same  $D/\lambda_C$  ratio would imply a  $\lambda_C = 80$  cm. This corresponds to a 12.5-MeV  $\gamma$  ray in liquid scintillator. The pair-production mean free path,  $\lambda_{p-p}$ , in liquid scintillator at 12.5 MeV is 270 cm.

We have a source to detector distance of 12 in. In the case of a 3-in. crystal, this corresponds to a source to crystal distance of 1.3 cm. The total intrinsic efficiency with this geometry for

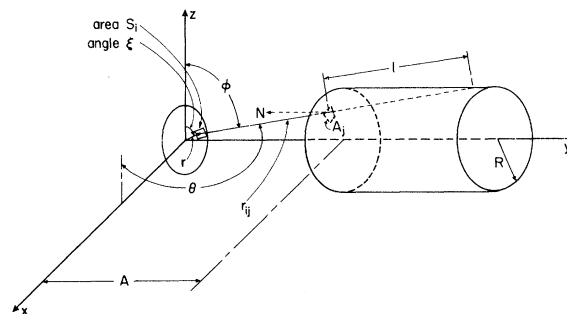


FIG. 19. Schematic diagram for solid-angle calculation with uranium source inside the shield.

0.5-MeV  $\gamma$  rays is given as 0.6.

If the energy of the  $\gamma$  ray which enters the liquid is increased, the Compton cross section decreases, while the pair-production cross section increases. As a result of this, we would not expect to see much of a change in efficiency of the detector over a considerable range in  $\gamma$  energy. Indeed, if similar calculations to the above are performed for  $\gamma$  energies up to 23 MeV, the efficiency remains approximately the same at 0.6.

#### 4. Self-Absorption of the Source

Our source was made up of a large number of thin disks of  $^{238}\text{U}$ . The thickness was kept small ( $\sim 0.16$  cm) to minimize self-absorption of the  $\gamma$  rays. We calculate that 86% of the  $\gamma$  rays  $> 8$  MeV do not lose energy in the source. Those that do are assumed to be removed from consideration.

### APPENDIX II: $\gamma$ AND NEUTRON ATTENUATION IN SHIELD

#### 1. $\gamma$ Attenuation

In order to calculate the  $\gamma$  attenuation in a shield, one must consider the results of a Compton collision. If, in such a collision, the resultant  $\gamma$  ray is so reduced in energy that it no longer exceeds the minimum discriminator setting, then this collision has resulted in the removal of the original  $\gamma$  ray. In addition, if the resultant  $\gamma$  ray has an energy above this minimum discriminator setting, but so reduced from the original  $\gamma$ -ray energy that its contribution to the bin it now finds itself in, is small compared to the number observed in that bin, then we can, in this case also, consider the  $\gamma$  ray removed.

Since our spectrum falls exponentially, we expect this last condition to hold for some range of

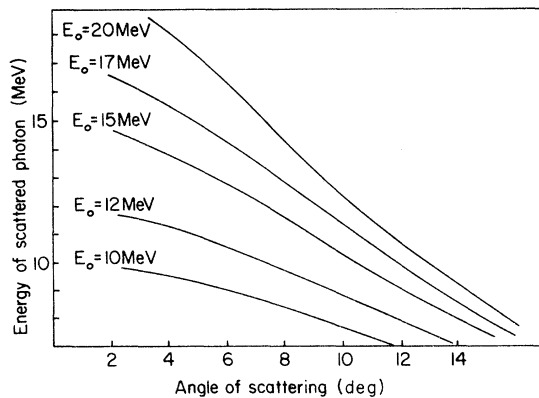


FIG. 20. Compton scattering (energy of scattered photon versus angle of scattering).

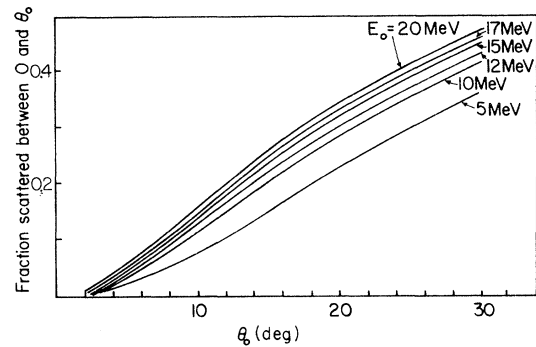


FIG. 21. Compton scattering. Fraction of photons scattered between 0 and  $\theta_0$  versus  $\theta_0$ , for various incident-photon energies.

scattering angles. For example, if the incoming  $\gamma$ -ray energy is 17 MeV, then if it is scattered at an angle greater than about  $16^\circ$ , its resultant energy will be below the discriminator setting of 8 MeV (Fig. 20). This accounts for 73.5% of the Compton collisions (Fig. 21). If it is scattered between  $10^\circ$  and  $11^\circ$ , it will go into the 11-MeV bin. About 2.1% of the collisions so scatter. This means that about 2.1% of the number incident upon the shield in the 17-MeV bin is to be compared with the number observed in the 11-MeV bin.

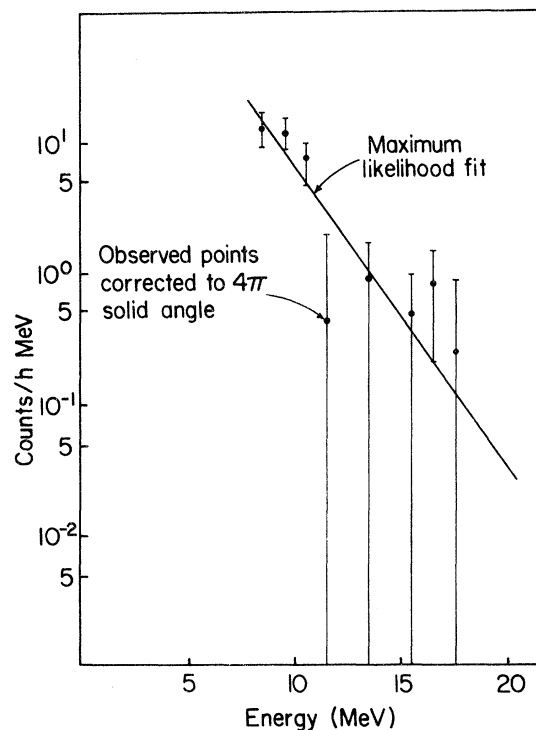


FIG. 22. The observed spectrum with uranium source outside the shield.

The original number in the 17-MeV bin is obtained from our observed spectrum when the uranium is inside the shield. We correct this spectrum to  $4\pi$  solid angle, and then say that this is the spectrum entering our shield. This curve was given as  $3.04 \times 10^4 e^{-E/1.45}$  (Fig. 8). To correct to  $4\pi$ , we multiply by  $1/0.319$  to get  $9.54 \times 10^4 e^{-E/1.45}$  counts/h MeV. The observed spectrum when the uranium is outside the shield and a maximum likelihood fit are plotted in Fig. 22.

In our example, we have

$$(0.021) (9.54 \times 10^4 e^{-17/1.45}) = (0.021) (0.7) = 0.0147/h$$

as the number scattered into the 11-MeV bin from the 17-MeV bin, and, from the maximum likelihood fit, 4.0/h as the number observed in the 11-MeV bin. Clearly, the 11-MeV bin is not influenced by this external source. By extension, anything scattered between 10 and 16° will show the same result. This means that, for an initial  $\gamma$  energy of 17 MeV, we are interested only in those  $\gamma$  rays scattered within about 10°. This is about 15% of the total number of Compton collisions, so, the appropriate cross section at 17 MeV is the total pair-production cross section plus 85% of the Compton cross section.

TABLE III. Maximum contributing scattering angle for various initial  $\gamma$ -energies.

	Bin energy	$\Delta\theta$	Fraction in $\Delta\theta$	$N(E_0)$ (Fraction in $\Delta\theta$ )	$N(E)$	$\frac{N(E_0) \text{ (Fraction in } \Delta\theta \text{)}}{N(E)}$
$E_0 = 10$ MeV $N(E_0) = 9.54 \times 10^4$	10	0-4	0.025	2.39	6.5	0.368
	9	4-8	0.055	5.25	12.0	0.438
	8	8-11	0.040	3.82	20.0	0.191
$E_0 = 12$ MeV $N(E_0) = 2.70 \times 10^4$	12	0-3	0.015	0.405	2.3	0.176
	11	3-6	0.040	1.080	4.0	0.270
	10	6-8	0.025	0.675	6.5	0.103
	9	8-10	0.045	1.220	12.0	0.102
	8	10-13	0.055	1.480	20.0	0.074
$E_0 = 15$ MeV $N(E_0) = 3.20 \times 10^0$	15	0-3	0.020	0.064	0.50	0.128
	14	3-5	0.030	0.096	0.85	0.113
	13	5-7	0.030	0.096	1.40	0.069
	12	7-8	0.020	0.064	2.30	0.028
	11	8-9	0.025	0.080	4.00	0.020
	10	9-11	0.035	0.112	6.5	0.017
	9	11-13	0.040	0.128	12.0	0.011
	8	13-15	0.040	0.128	20.0	0.006
$E_0 = 17$ MeV $N(E_0) = 7.0 \times 10^{-1}$	17	0-2	0.008	0.0056	0.17	0.033
	16	2-4	0.029	0.0203	0.30	0.066
	15	4-6	0.031	0.0217	0.50	0.043
	14	6-7	0.018	0.0126	0.85	0.015
	13	7-8	0.023	0.0161	1.40	0.012
	12	8-10	0.040	0.0280	2.30	0.012
	11	10-11	0.021	0.1470	4.00	0.004
	10	11-12	0.020	0.0140	6.50	0.002
	9	12-14	0.040	0.0280	12.00	0.002
	8	14-16	0.035	0.0245	20.00	0.001
$E_0 = 20$ MeV $N(E_0) = 9.54 \times 10^{-2}$	20	0-2	0.010	0.0009	0.035	0.0260
	19	2-4	0.025	0.0024	0.060	0.0400
	18	4-5	0.020	0.0019	0.100	0.0190
	17	5-6	0.020	0.0019	0.170	0.0110
	16	6-7	0.015	0.0014	0.300	0.0050
	15	7-8	0.030	0.0029	0.500	0.0060
	14	8-9	0.020	0.0019	0.85	0.0020
	13	9-10	0.020	0.0019	1.40	0.0010
	12	10-11	0.025	0.0024	2.30	0.0010
	11	11-12	0.020	0.0019	4.00	0.0005
	10	12-13	0.020	0.0019	6.50	0.0003
	9	13-15	0.035	0.0033	12.00	0.0003
	8	15-17	0.035	0.0033	20.00	0.0002

TABLE IV. Mass attenuation coefficients for Compton scattering in wax and boric acid.

Energy (MeV)	$\mu/\rho$	$\mu/\rho$
	Wax (CH <sub>2</sub> ) Z/A = 0.572	Boric acid (H <sub>3</sub> BO <sub>3</sub> ) Z/A = 0.5175
10	0.01735	0.01574
12	0.01524	0.01380
15	0.01293	0.01172
17	0.01155	0.01047
20	0.01023	0.00927

Figure 21 is the fraction of  $\gamma$  rays Compton scattered between 0 and  $\theta_0$  as a function of  $\theta_0$ . This was obtained by integrating  $(d\sigma^{\theta_0}/d\Omega)/(d\sigma^{\pi}/d\Omega)$  and evaluating the result for various values of  $\theta_0$  and incoming  $\gamma$  energy.

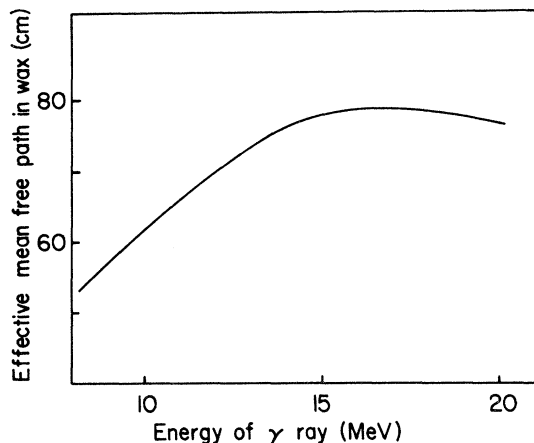
In Table III, we calculate the maximum contributing scattering angle for various initial  $\gamma$  energies. Here, we assume that if the fraction scattered into a bin is less than 1% of the number observed in that bin, we can ignore this contribution. Thus, Table III says that 10-MeV  $\gamma$  rays will contribute to our observed signal until we reach a scattering angle of 11°. For 12-MeV  $\gamma$  rays, this angle is 13°; for 15-MeV  $\gamma$  rays, 15°; for 17-MeV  $\gamma$  rays, 10°; and for 20-MeV  $\gamma$  rays, 6°.

In Table IV, we list the mass attenuation coefficients for wax and boric acid. In Tables V and VI, we calculate the effective mean free path in wax and boric acid. These are plotted in Figs. 23 and 24. In Table VII, we calculate the total attenuation in our shield consisting of 3 ft of wax and 2 in. of boric acid.

Using these calculated attenuations, we can predict the spectrum that we should observe if only  $\gamma$ -ray attenuation were responsible. We do this by modifying the spectrum we obtained with the uranium inside the shield corrected for solid angle. This is plotted in Fig. 12.

## 2. Neutron Attenuation

The following processes contribute to the attenuation of a fast neutron in a shield: isotropic elas-

FIG. 23. Effective mean free path of  $\gamma$  rays in wax versus  $\gamma$  energy.

tic scattering with a light element, inelastic scattering, and part of the shadow-scattering cross section.

Our shield is a particularly good neutron attenuator, since it contains a large amount of hydrogen. Since hydrogen has a steep increase in cross section with decreasing neutron energy, and since a collision usually results in a large energy loss, we can consider a neutron to be removed if it undergoes a collision with hydrogen. If other materials are present in the shield, their effectiveness is increased, since a neutron scattered off this material has a larger probability of a hydrogen collision.

For elements other than hydrogen, an effective removal cross section is defined as that cross section necessary to get the right answer for fast-neutron attenuation. This varies with neutron energy, but is approximately constant over the range with which we are working. The effective removal cross section is only justified when a shield contains an appreciable amount of hydrogen. Its value, typically, is about 40% below the total cross section. In our shield, (CH<sub>2</sub>), the effective removal cross section for carbon is 0.81 b/atom.<sup>14</sup>

The mean free path, as a function of neutron

TABLE V. Effective mean free path of  $\gamma$  rays in wax.

$E$ (MeV)	(Compton $\mu/\rho$ ) (Fraction effective)	$\mu/\rho$ Pair production	Effective total $\mu/\rho$	Effective $\lambda$ (cm)
10	(0.01735) (0.87) = 0.0151	0.0036	0.0187	61.6
12	(0.01524) (0.82) = 0.0125	0.0040	0.0165	69.9
15	(0.01293) (0.76) = 0.0098	0.0047	0.0145	79.5
17	(0.01155) (0.85) = 0.0098	0.0053	0.0151	76.3
20	(0.01023) (0.93) = 0.0095	0.0055	0.0150	76.8

TABLE VI. Effective mean free path of  $\gamma$  rays in boric acid.

$E$ (MeV)	(Compton $\mu/\rho$ ) (Fraction effective)	$\mu/\rho$ Pair production	Effective total $\mu/\rho$	Effective $\lambda$ (cm)
10	(0.015 74) (0.87) = 0.0137	0.0048	0.0185	52.5
12	(0.013 80) (0.82) = 0.0113	0.0053	0.0166	58.5
15	(0.011 72) (0.76) = 0.0089	0.0059	0.0148	65.6
17	(0.010 47) (0.85) = 0.0088	0.0065	0.0153	63.5
20	(0.009 27) (0.93) = 0.0086	0.0071	0.0157	61.8

energy, and the attenuation in our shield, is calculated in Table VIII.

Using these calculated neutron attenuations, we predict the spectrum that should be observed if only neutron attenuation were responsible. This, also, is plotted in Fig. 12.

#### APPENDIX III: NEUTRON CAPTURE PROBABILITIES

Let us ignore the iron for the moment and look at the observed  $\gamma$  spectrum in the detector with energy  $\geq 8.5$  MeV. Since the  $\gamma$  rays from thermal-neutron capture in  $^{28}\text{Si}$  and aluminum are 8.5 and 7.7 MeV, respectively, the Pu-Be neutrons need only be of thermal energy, while the uranium neutrons must be 0.8 MeV.

In the case of aluminum, the cross section for neutron absorption [ $^{27}\text{Al}(n, \gamma)^{28}\text{Al}$ ] for a neutron energy of 0.8 MeV is 0.002 b.<sup>15</sup> We use this cross section, and not simply the cross section for production of any  $\gamma$  rays, because we are interested only in production of  $\gamma$  rays with an energy of 8.5 MeV. The  $(n, X\gamma)$  cross section, for example,

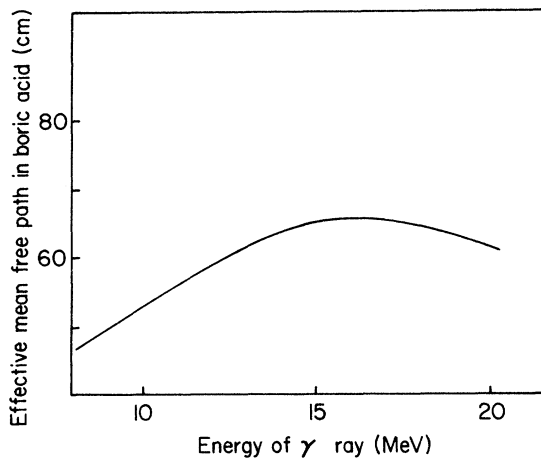


FIG. 24. Effective mean free path of  $\gamma$  rays in boric acid versus  $\gamma$  energy.

includes  $\gamma$  rays produced in  $(n, n')$  reactions where the only energy available to the  $\gamma$  ray is the incident-neutron kinetic energy.

Our aluminum wall thickness is 0.178 cm. Since the source emits neutrons isotropically, a somewhat larger average path length (0.28 cm) is seen by the neutrons in passing through the aluminum wall.

The fraction of neutrons that interact in this average path length =  $1 - e^{-0.28/\lambda}$  where,

$$\lambda = \frac{A}{\rho N_0 \sigma} = \frac{27}{(2.7) (6.03 \times 10^{23}) (2 \times 10^{-27})},$$

$$\lambda = 8.2 \times 10^3 \text{ cm}.$$

So, the fraction is  $3.41 \times 10^{-5}$ .

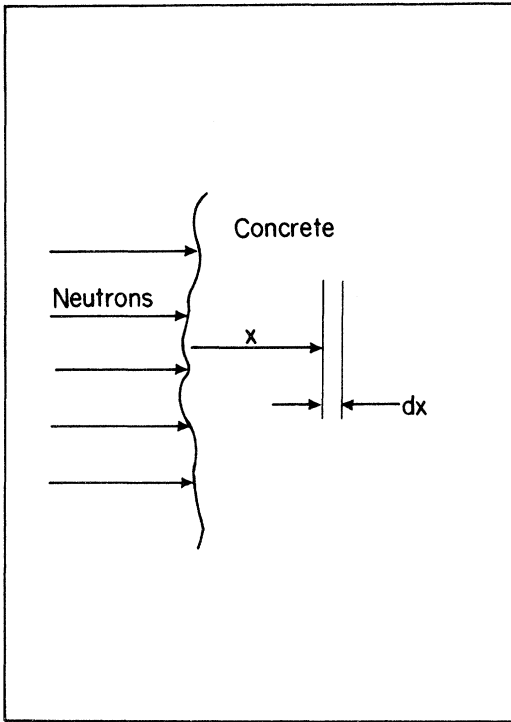
Let us now consider neutrons entering the rock (Fig. 25). We are interested in neutrons that undergo the  $^{28}\text{Si}(n, \gamma)^{29}\text{Si}$  reaction; however, in traversing the rock, the neutrons are attenuated by other processes. We note that: (i) The fraction of incoming neutrons that traverses a rock distance  $X$  without interacting is  $e^{-X/\lambda_1}$ ; (ii) the fraction that interacts [ $^{28}\text{Si}(n, \gamma)^{29}\text{Si}$ ] in a thickness  $dX$  is  $(dX)/\lambda_2$ ; (iii) the fraction of the  $\gamma$  rays produced in  $dX$  that are capable of getting through rock a distance  $X$  is  $e^{-X/\lambda_3}$ .

So, the fraction of  $\gamma$  rays due to the incoming neutron beam that escape the rock is

$$\int_0^\infty \frac{e^{-X/\lambda_1} e^{-X/\lambda_3}}{\lambda_2} dX = \frac{1}{\lambda_2} \left[ \frac{\lambda_1 \lambda_3}{\lambda_1 + \lambda_3} \right].$$

TABLE VII. Attenuation of  $\gamma$  rays in a 3-ft wax and boric acid shield.

Energy (MeV)	Total attenuation
10	(4.41) (1.10) = 4.85
12	(3.70) (1.09) = 4.04
15	(3.16) (1.08) = 3.41
17	(3.32) (1.08) = 3.58
20	(3.29) (1.08) = 3.56

FIG. 25. Neutrons capturing in  $^{28}\text{Si}$ .

For thermal  $n$ 's, the total neutron cross section for  $^{16}\text{O} = 3.6$  b and the total neutron cross section for Si = 1.5 b.<sup>15</sup> Thus for rock ( $\text{SiO}_2$ ):

$$\begin{aligned}\Sigma &= \frac{\rho N_0}{A} [\sigma_{\text{Si}} + 2\sigma_{^{16}\text{O}}] \\ &= \frac{(2.8)(6.03 \times 10^{23})}{60} [1.5 + 2(3.6)] \times 10^{-24} \\ &= 2.45 \times 10^{-1} \text{ cm}^{-1}.\end{aligned}$$

So,  $\lambda_1 = 1/\Sigma = 4.08$  cm is the mean free path for absorbing or scattering the neutrons before they reach the thickness  $dX$ .

In the silicon, the thermal-neutron-capture cross section is 0.13 b, while for  $^{16}\text{O}$ ,  $< 0.0002$  b.<sup>14</sup> Then for  $\text{SiO}_2$

$$\begin{aligned}\Sigma &= \frac{\rho N_0 \sigma}{A} = \frac{(2.8)(6.03 \times 10^{23})(0.13 \times 10^{-24})}{60} \\ &= 3.64 \times 10^{-3} \text{ cm}^{-1},\end{aligned}$$

TABLE VIII. Neutron attenuation in a 3-ft wax shield.

Energy (MeV)	$\sigma_H$ (b)	$\sigma_c$ (b)	$\Sigma$ ( $\text{cm}^{-1}$ )	$\lambda$ (cm)	Attenuation
8	1.12	0.81	$1.14 \times 10^{-1}$	8.7	$3.3 \times 10^4$
10	0.95	0.81	$1.01 \times 10^{-1}$	9.9	$1.0 \times 10^4$
12	0.82	0.81	$9.16 \times 10^{-2}$	10.9	$4.4 \times 10^3$
15	0.69	0.81	$8.20 \times 10^{-2}$	12.2	$1.8 \times 10^3$

and  $\lambda_2 = 1/\Sigma = 2.75 \times 10^2$  cm is the mean free path for the reaction  $^{28}\text{Si}(n, \gamma)^{29}\text{Si}$ .

The  $\gamma$  rays so produced in the rock have a mean free path  $\lambda_3 = 14.95$  cm determined as follows:

$$\frac{\mu}{\rho} = \frac{\mu_1}{\rho_1} w_1 + \frac{\mu_2}{\rho_2} w_2,$$

where  $\mu_i/\rho_i$  is the mass attenuation coefficient<sup>16</sup> and  $w_i$  is the fraction by weight of element  $i$  since

$$\frac{\mu}{\rho} = 0.0254(0.467) + 0.0224(0.534),$$

$$\mu = 2.8(0.0239) + 0.0669,$$

we get  $\lambda_3 = 1/\mu = 14.95$  cm is the mean free path of 8.5-MeV  $\gamma$  rays in  $\text{SiO}_2$ .

Thus, substituting into the above,

$$\frac{1}{\lambda_2} \left[ \frac{\lambda_1 \lambda_3}{\lambda_1 + \lambda_3} \right] = \frac{1}{275} \frac{4.08(14.95)}{4.08 + 14.95} = 1.16 \times 10^{-2}.$$

We have then, that the ratio of the probabilities of producing observable  $\gamma$  rays in these two cases is:

$$\frac{\text{Prob. of } \gamma\text{'s due to Pu-Be}}{\text{Prob. of } \gamma\text{'s due to uranium}} = \frac{1.16 \times 10^{-2}}{3.41 \times 10^{-5}} = 3.4 \times 10^2.$$

#### ACKNOWLEDGMENTS

We sincerely thank the directors and staff of the East Rand Proprietary Mine for their generous hospitality and assistance. M. Stein and G. Nelson gave valuable assistance in film scanning and interpretation. B. Shoffner designed a portion of the electronics.

<sup>†</sup>Work supported in part by the U. S. Atomic Energy Commission.

<sup>\*</sup>Now at the Weizmann Institute, Rehovoth, Israel.

<sup>1</sup>This predicted flux at the earth has since been lowered to at most  $2 \times 10^6$  neutrinos  $\text{cm}^{-2} \text{sec}^{-1}$  by R. Davis, Jr., Phys. Rev. Lett. **12**, 303 (1964); R. Davis, Jr., D. S. Harmer, and K. C.

Hoffman, Phys. Rev. Lett. **20**, 1205 (1968); R. Davis, Jr., L. C. Rogers, and V. Rodeka, Bull. Am. Phys. Soc. **16**, 631 (1971).

<sup>2</sup>National Institute for Metallurgy, Johannesburg, South Africa.

<sup>3</sup>R. L. Gamble, ORNL Report No. ORNL-1620, 1953

(unpublished); Francis and Gamble, ORNL Report No. ORNL-1879, 1955 (unpublished), p. 20.

<sup>4</sup>F. C. Maienschein, R. W. Peele, W. Zobel, and T. A. Love, in *Proceedings of the Second United Nations International Conference on the Peaceful Uses of Atomic Energy* (United Nations, Geneva, 1958), Vol. 15, p. 366; R. W. Peele and F. C. Maienschein, *Phys. Rev. C* **3**, 373 (1971).

<sup>5</sup>M. F. Crouch, H. S. Gurr, A. A. Hruschka, T. L. Jenkins, W. R. Kropp, F. Reines, and H. Sobel, *IEEE Trans. Nucl. Sci.*, NS-13, No. 3 (1966).

<sup>6</sup>H. S. Gurr, Ph.D. thesis, Case Institute of Technology, 1966 (unpublished), p. 42.

<sup>7</sup>Price, Horton, and Spinney, *Radiation Shielding* (Pergamon, New York, 1957), p. 135.

<sup>8</sup>P. M. Endt and C. van der Leun, *Nucl. Phys.* **A105**, 1(1967).

<sup>9</sup>For details, see H. W. Sobel, Ph.D. thesis, Case Institute of Technology, 1969 (unpublished).

<sup>10</sup>Evans, *The Atomic Nucleus* (McGraw-Hill, New York, 1955), p. 390.

<sup>11</sup>F. B. Harrison, *Nucleonics* **10**, 40 (1952).

<sup>12</sup>J. W. Brooks and F. Reines, following paper, *Phys. Rev. C* **7**, 1579 (1973).

<sup>13</sup>A. H. Snell, *Nuclear Instruments and Their Uses* (Wiley, New York, 1962), p. 342.

<sup>14</sup>See Ref. 7, p. 180.

<sup>15</sup>UCRL Report No. UCRL-5226.

<sup>16</sup>G. W. Grodstein, National Bureau of Standards, Circular No. 583 (1957).

## Fragment-Mass Ratios in $^{252}\text{Cf}$ Fission Versus Prompt Gamma-Ray Energy\*

J. W. Brooks, Jr., and F. Reines

University of California, Irvine, California 92664

(Received 17 August 1972)

$\gamma$  rays associated with the spontaneous fission of  $^{252}\text{Cf}$  have been observed in the energy range 10–16 MeV using two 7.6-cm-by-29.2-cm-diam NaI(Tl) crystals in coincidence with two solid-state fission counters. Evidence is presented for a  $\gamma$  ray multiplicity of 2 implying the presence of a collective mode of fragment deexcitation. The fission-fragment-mass-ratio distribution shows an increase in the number of symmetric fissions when the detected  $\gamma$  energy exceeds 14 MeV. It is suggested that deexcitation of the fragments by the giant dipole resonance may be responsible for the presence of the high-energy  $\gamma$  rays.

### I. INTRODUCTION

In the past decade studies of the energy balance in the fission process have become increasingly complex and sophisticated. Many data have been obtained concerning x rays,  $\gamma$  rays, neutrons, and their yields, multiplicities, and correlations with fragment-mass ratio.<sup>1-8</sup> Until a few years ago  $\gamma$ -ray measurements extended to energies  $\sim 8$  MeV. In 1968, an experiment was performed by Sobel *et al.*<sup>9</sup> which measured the  $\gamma$  spectrum from the spontaneous fission of  $^{238}\text{U}$  in the energy range 8–20 MeV.

The experiment described in this paper is based on work done at the University of California at Irvine for a doctoral thesis and extends the work of Sobel *et al.* by measuring fission-fragment-mass ratios in coincidence with the  $\gamma$  rays. In the Sobel experiment a 10-kg  $^{238}\text{U}$  source was used in conjunction with a large liquid scintillation detector located about 3 km underground. The large amount of  $^{238}\text{U}$  and the attendant complications were dictated by its long half-life for spontaneous fission. In this experiment we investigate the high-energy  $\gamma$  rays arising from the fission of  $^{252}\text{Cf}$ , a much more accessible process because of the

short half-life for spontaneous fission (85 yr). Briefly, the apparatus for the experiment consists of two solid-state fragment detectors mounted on either side of the  $^{252}\text{Cf}$  source, all of which is enclosed in a vacuum chamber. Two large NaI crystals are employed to observe the  $\gamma$  rays.

The short half-life for  $^{252}\text{Cf}$  spontaneous fission results in several advantages. First, only microgram quantities of  $^{252}\text{Cf}$  are needed to obtain the necessary source strength. This small amount can be deposited in a very thin layer which makes possible the detection and energy measurement of the fragments. In consequence, we can obtain data on the fission fragments and the associated  $\gamma$  rays from a fission event. Finally, the small size coupled with the distinctive fission-fragment pulses makes it unnecessary to place the apparatus deep underground to be rid of the cosmic-ray background.

The study of fragment-mass ratios and high-energy  $\gamma$  rays described below may provide some information about what is happening near the point of scission such as the shape of the nucleus and how it divides. Further, the study of prompt high-energy  $\gamma$  rays is expected to provide information on the deexcitation of very highly deformed nuclei